How to cite: *Angew. Chem. Int. Ed.* **2025**, *64*, e202422744
doi.org/10.1002/anie.202422744

CO2 Hydrogenation to Ethanol

Exceptional CO_2 Hydrogenation to Ethanol via Precise Single-Atom Ir Deposition on Functional P Islands

Lingyue Liu[+], Jinjie Liu[+], Guangchao Li, Xiuwen Shi, Jun Yin, Shourong Zheng, Ka-Fu Yung,* Hong Bin Yang,* and Tsz Woon Benedict Lo**

Abstract: The thermocatalytic hydrogenation of CO_2 to ethanol has attracted significant interest because ethanol offers ease of transport and substantial value in chemical synthesis. Here, we present a state-of-the-art catalyst for the CO_2 hydrogenation to ethanol achieved by precisely depositing single-atom Ir species on P cluster islands situated on the In_2O_3 nanosheets. The Ir_1-P_x/In_2O_3 catalyst achieves an impressive ethanol yield of 3.33 mmol g^{-1} h^{-1} and a turnover frequency (TOF) of 914 h^{-1} under 1.0 MPa (H_2/CO_2 = 3:1) at 180 °C, nearly 8 times higher than that of the unmodified Ir_1/In_2O_3 catalyst. Additionally, at a more industrially relevant pressure of 5.0 MPa, the TOF of the Ir_1-P_x/In_2O_3 catalyst can reach up to 2108 h^{-1}, surpassing previously reported catalysts. Combined in situ characterization and theoretical studies reveal that the hydrogenation process is significantly enhanced by the Ir_1-P_x entities. Specifically, the Ir atom facilitates CO_2 activation and C–C coupling, while the surrounding P island exhibits exceptional H_2 dissociation ability. These three steps have been found crucial for the CO_2 hydrogenation reaction. This discovery opens new opportunities for the regulation of the microenvironment of current catalysts by providing essential chemical functionalities that enhance intricate and complex reaction processes.

[*] Dr. L. Liu,[+] Dr. G. Li, Prof. K.-F. Yung, Prof. T. W. B. Lo
State Key Laboratory of Chemical Biology and Drug Discovery
Department of Applied Biology and Chemical Technology
The Hong Kong Polytechnic University
Hung Hom, Kowloon, Hong Kong, 100872, China
E-mail: kf.yung@polyu.edu.hk
benedict.tw.lo@polyu.edu.hk

Prof. S. Zheng
School of the Environment
Nanjing University
Nanjing, 210046, China

J. Liu,[+] Prof. J. Yin
Department of Applied Physics
The Hong Kong Polytechnic University
Hung Hom, Kowloon, Hong Kong, 100872, China
E-mail: jun.yin@polyu.edu.hk

X. Shi, Prof. H. B. Yang
School of Materials Science and Engineering
Suzhou University of Science and Technology
Suzhou 215009, China
E-mail: yanghb@usts.edu.cn

Prof. K.-F. Yung, Prof. T. W. B. Lo
The Hong Kong Polytechnic University Shenzhen Research Institute
The Hong Kong Polytechnic University
Shenzhen 518057, China

Prof. K.-F. Yung, Prof. T. W. B. Lo
PolyU-Daya Bay Technology and Innovation Research Institute
The Hong Kong Polytechnic University
Huizhou, Guangdong, China

[+] Contributed equally to this work.

Introduction

The sequestration and conversion of excess CO_2 have emerged as pivotal focal points in the strategic agendas of numerous nations due to the urgent need to address climate change and environmental degradation.[1] Among the various approaches, the thermocatalytic hydrogenation of CO_2 to ethanol (or other higher alcohols) has garnered significant interest owing to the ease of transport and their substantial value in chemical synthesis.[2] The process of CO_2 hydrogenation to ethanol is highly intricate, involving the activation and reduction of CO_2, activation of H_2, and facilitation of C–C coupling.[3] Consequently, it poses a significant challenge for catalyst design. Ongoing advancements in catalysis and chemical engineering are necessary to render the process economically and environmentally feasible, with a focus on achieving reactions at lower pressures while maximizing catalyst atom efficiency.[4]

Recently, metal-based single-atom catalysts (SACs) have taken the spotlight in studies on the thermocatalytic hydrogenation of CO_2 to ethanol.[5] These SACs capitalize on the collaboration between the precisely defined 'single-atom' metal center and the electronic and geometric interactions with the support surface. Notably, Huang et al. achieved remarkable CO_2-to-ethanol activity by anchoring single-atom Ir species onto the surface of In_2O_3, featuring a high turnover frequency (TOF) of 481 h^{-1} for each Ir atom.[6] This success highlights the effective synergy between the adsorption and activation of CO_2 by the Ir sites and the In_2O_3 supports with oxygen vacancies. However, challenges arise in this system as the Ir sites fulfil multiple roles, potentially leading to their saturation during catalysis, there-

by impeding the kinetic processes of CO_2 and H_2 activations and impacting overall catalytic activity.

While SACs have shown promise, ensuring stable metal centers on the support surface while maintaining structural flexibility for completing the catalytic cycle remains a critical challenge. The essential chemical bonding between the metal center and the support carrier, vital for preventing metal detachment or aggregation, often results in a spatially constrained environment that limits the activation of complex or multiple substrates concurrently.[7] The efficacy of single-atom metal sites for intricate molecular transformations has sparked debates within the scientific community, with some researchers advocating for tailored tertiary or microenvironments that could enhance efficiency, particularly when multiple functional motifs are at play.[8] Alternatively, exploring potential synergies among atomic-level active sites during design optimization to target specific steps without compromising other functions presents an intriguing avenue for further exploration in catalytic design.[9]

In this study, we demonstrate a synthetic strategy involving the deposition of phosphorus cluster islands ('P islands') onto In_2O_3 nanosheets. These P islands serve as hosts for single Ir atoms, leading to the formation of 'Ir_1-P_x' on In_2O_3 nanosheets (Ir_1-P_x/In_2O_3). The specific coordination of the Ir center with the P islands not only alters the electronic structure of the Ir center, optimizing the adsorption and activation of CO_2 molecules as well as their C–C coupling ability but also the P atoms exhibit excellent H_2 dissociation ability compared to the Ir single atomic site in Ir_1/In_2O_3. Overall, the presence of these Ir_1-P_x entities in Ir_1-P_x/In_2O_3 effectively enhances the TOF for each Ir atom by 7.8 times compared to unmodified Ir_1/In_2O_3. The discovery presents novel opportunities for the development of 'next-generation' SACs, which are essential for intricate chemical reactions.

Results and Discussion

Synthesis and Structural Characterizations of Ir_1-P_x/In_2O_3

The Ir_1-P_x/In_2O_3 catalyst, which features atomically dispersed Ir deposited onto P islands and supported on ultrathin In_2O_3 nanosheets, via a three-step-process, as summarized in Figure 1a. First, the In_2O_3 nanosheets were obtained by annealing $In(C_{17}H_{33}COO)_3$ precursor at 400 °C for 3 min, following the established method in the literature (Figure S1).[10] Second, the phosphorization of these ultrathin In_2O_3 nanosheets was conducted at 400 °C to produce P-In_2O_3, where the phosphorus species form small cluster islands on the support surface as previously documented.[11] Finally, the Ir precursor (H_2IrCl_6) was impregnated onto P-In_2O_3, and the target catalyst (Ir_1-P_x/In_2O_3) was obtained through hydrogen reduction (5 % H_2 / 95 % Ar) at 300 °C. A control sample, Ir_1/In_2O_3, was prepared without P modification, as detailed in the Supporting Information and the catalyst preparation section (see Figure S1a and S1b). Interestingly, the introduction of P results in a significant reduction in the single electron signal of In_2O_3 (Figure S2), which should be attributed to P clusters covering the oxygen vacancies in In_2O_3. The Ir contents of Ir_1/In_2O_3 and Ir_1-P_x/In_2O_3 were determined as 0.13 wt %, and 0.07 wt %, respectively (Table S1).

The powder X-ray diffraction (XRD) patterns of the prepared samples, shown in Figure 1b, reveal only the characteristic diffraction peaks attributed to cubic In_2O_3 with the space group of I_{213} ($a = 10.1296(7)$ Å; JCPDS#88-2160). The Pawley refinement profile of Ir_1-P_x/In_2O_3 is presented in Figure 1c and the structural parameters are summarized in Table S2 (refinement profiles of other samples are shown in Figure S3). The absence of P-related peaks in P-In_2O_3 and Ir_1-P_x/In_2O_3 suggests that phosphorus does not exist in In_2O_3 in the form of crystalline metal phosphides or phosphorus species. Furthermore, no Ir-related peaks were detected in Ir_1-P_x/In_2O_3 and Ir_1/In_2O_3, indicating that Ir species are likely atomically dispersed.

The transmission electron microscopy (TEM) images (Figure S4) reveal the size of the In_2O_3 nanosheets is approximately 10 nm. Furthermore, phosphorus modification and the immobilization of Ir species did not alter the morphological characteristics of the In_2O_3 nanosheets, as depicted in Figure S5–S6. The scanning transmission electron microscopy (STEM) energy dispersive X-ray spectroscopy (EDX) mapping and line profile for the Ir_1-P_x/In_2O_3 show a uniform distribution of In, O, P, and Ir atoms throughout the sample (Figure 1d–e). High-angle angular dark-field (HAADF) STEM was further employed to identify the states of Ir species on the surfaces of P-In_2O_3 and In_2O_3. The HAADF-STEM images of In_2O_3 and Ir_1-P_x/In_2O_3 (Figure 1f–g) exhibit well-defined crystal structures, displaying regular lattice fringes with a d-spacing of 2.3 Å, corresponding to (222) of cubic In_2O_3 nanosheets. In contrast to Figure 1f, bright spots observed in Figure 1g can be attributed to atomically dispersed Ir species. Importantly, no Ir clusters were detected in the HAADF-STEM images, which is consistent with our diffraction evidence.

To study the oxidation states and coordination environment of these atomically dispersed Ir species in Ir_1/In_2O_3 in Ir_1-P_x/In_2O_3, X-ray absorption spectroscopy measurements were conducted.[12] The normalized Ir L_3-edge X-ray absorption near-edge spectroscopy (XANES) (Figure 2a) shows that the white-line intensities of Ir_1/In_2O_3 and Ir_1-P_x/In_2O_3 samples fall between those of Ir foil and IrO_2, indicating that the oxidation number of the Ir species in both samples is +2, as determined by a linear combination fit (inset of Figure 2a), with the valence state in Ir_1-P_x/In_2O_3 being slightly higher.[8b,13] Further analysis using extended X-ray absorption fine structure (EXAFS) studies the local coordination environment of Ir atoms, complementing the structural findings. The wavelet transform (WT) analysis of the EXAFS data for Ir_1/In_2O_3 (Figure 2b) shows a strong lobe centered at $k = 5.5$ Å^{-1} and R ~1.5 Å, corresponding to the oxygen atoms surrounding the Ir center. In contrast, for Ir_1-P_x/In_2O_3 (Figure 2c), the lobe shifts to higher k and R values, specifically at $k = 7.5$ Å^{-1} and R ~1.7 Å, indicating coordination of Ir to heavier P atoms. The subsequent Fourier-transformed EXAFS data (Figure 2d) reveal only

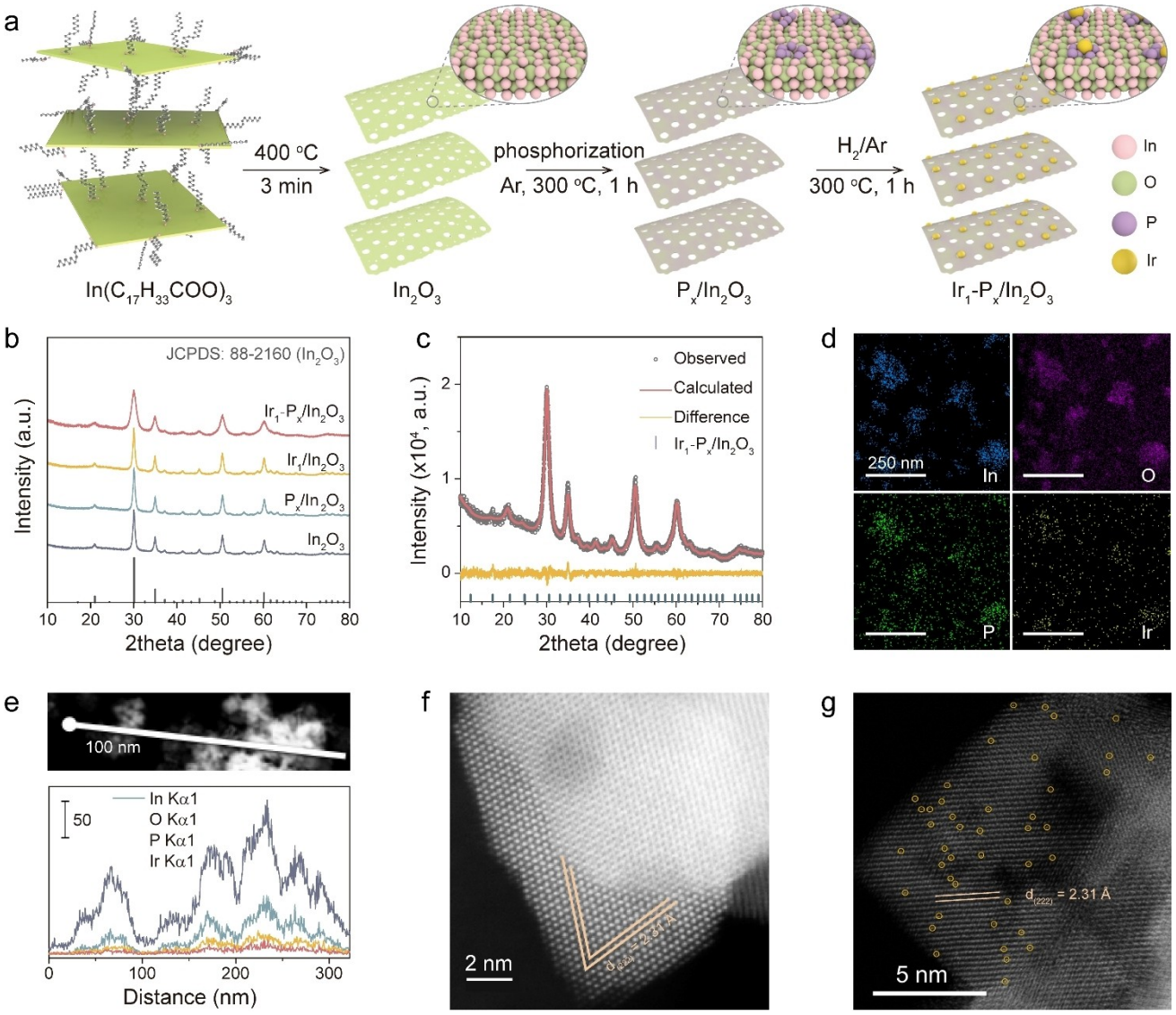

Figure 1. (a) Synthesis Scheme of Ir_1-P_x/In_2O_3. (b) Powder XRD patterns of In_2O_3, P-In_2O_3, Ir_1/In_2O_3, and Ir_1-P_x/In_2O_3 (λ = 1.5418 Å). (c) The Pawley refinement profile of Ir_1-P_x/In_2O_3. (d) EDX elemental mapping images, and (e) STEM-EDX line profile of Ir_1-P_x/In_2O_3. HAADF-STEM images of (f) In_2O_3, and (g) Ir_1-P_x/In_2O_3.

one characteristic peak in both Ir_1/In_2O_3 and Ir_1-P_x/In_2O_3, corresponding to the Ir–O and Ir–P backscattering paths in the first shell. Notably, no first-shell Ir–O contribution was observed in Ir_1-P_x/In_2O_3. The absence of a peak around 2.4 Å, which would indicate an Ir–Ir scattering path present in Ir foil, further confirms that the Ir atoms are atomically dispersed on the respective support surfaces. From the quantitative fitting analysis (Figure 2e–f and Figure S7; detailed EXAFS parameters are provided in Table S3), the Ir–O scattering path in Ir_1/In_2O_3 is calculated to be 1.98 Å, with an average coordination number of 4.6. Conversely, the Ir–P scattering path in Ir_1-P_x/In_2O_3 is calculated to be 2.28 Å, with an average coordination number of 3.7. It is noteworthy that the scattering path characteristic of Ir–O at ~2 Å is absent. This indicates that Ir is directly immobilized on the In_2O_3 support in Ir_1/In_2O_3, whereas in Ir_1-P_x/In_2O_3, Ir is distinctly deposited onto the P islands without direct contact with the In_2O_3 support. Our density functional theory (DFT) calculations (shown in the insets of Figure 2e and 2f) suggest that the formation energies for Ir immobilization on In_2O_3 and P-In_2O_3 are −10.3 eV and −7.7 eV, respectively, indicating thermodynamically stable Ir immobilization as a 'single atom'.

X-ray photoelectron spectroscopy (XPS) further elucidated the electronic properties of the Ir(II) species. Figure 2g–i and Figure S8 present the high-resolution XPS spectra for Ir 4*f*, In 3*d*, P 2*p*, and O 1s of the samples. The binding energy of the Ir 4*f* in Ir_1-P_x/In_2O_3 is higher than that of Ir_1/In_2O_3, with values of $4f_{7/2}$ = 62.1 eV and $4f_{5/2}$ = 64.8 eV for Ir_1-P_x/In_2O_3 (compared to $4f_{7/2}$ = 62.4 eV and $4f_{5/2}$ = 65.1 eV for Ir_1-P_x/In_2O_3). This indicates a slightly higher valence state of Ir(II) in Ir_1-P_x/In_2O_3 (Figure 2i), aligning well with our findings from XANES.[14] Additionally, the binding energy of In 3*d* exhibits a blue shift when Ir atoms

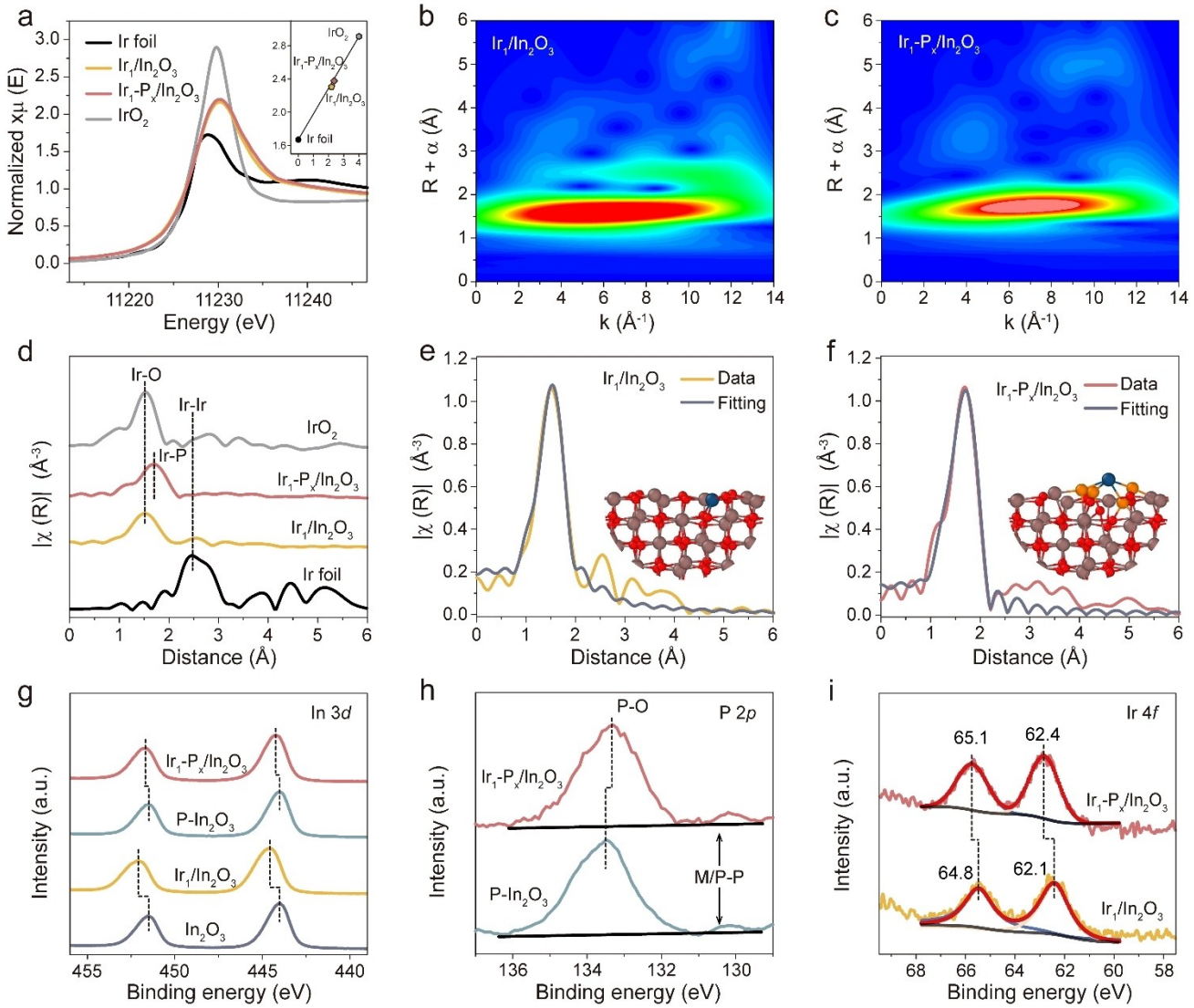

Figure 2. (a) Ir L_3-edge XANES spectra for Ir foil, IrO_2, Ir_1/In_2O_3 and Ir_1-P_x/In_2O_3. Wavelet transforms for the k^2-weighted EXAFS data of (b) Ir_1/In_2O_3 and (c) Ir_1-P_x/In_2O_3. (d) Ir L_3-edge FT-EXAFS for Ir foil, IrO_2, Ir_1/In_2O_3 and Ir_1-P_x/In_2O_3. Ir L_3-edge EXAFS spectra and the corresponding curve-fits in R-space of (e) Ir_1/In_2O_3 and (f) Ir_1-P_x/In_2O_3 (inset: DFT-optimized crystal structures). High-resolution X-ray photoelectron spectra for the (g) In 3*d*, (h) P 2*p*, and (i) Ir 4*f* states for Ir_1/In_2O_3, and Ir_1-P_x/In_2O_3.

are loaded onto the surfaces of In_2O_3 (by 0.5 eV) and P-In_2O_3 (by 0.3 eV). In contrast, simple P modification on In_2O_3 does not change the binding energy of In 3*d*. The P 2*p* XPS dataset in Figure 2h shows the phosphorus species in both P-In_2O_3 and Ir_1-P_x/In_2O_3 exhibit two chemical states: oxidized phosphorus species at 133.10 eV and metal/P–P(in the form of P cluster) at approximately 130.0 eV, and the intensity of metal/P–P peak for Ir_1-P_x/In_2O_3 slightly higher than that of P-In_2O_3.[15] The combined evidence suggests that in Ir_1-P_x/In_2O_3, the Ir atoms are directly immobilized on the P_x islands on the In_2O_3 surface through the formation of Ir–P bond.[16]

CO_2 Hydrogenation Performance of Ir_1-P_x/In_2O_3

The CO_2 hydrogenation catalytic performance of these samples was evaluated in a stainless-steel autoclave, with the following reaction conditions: 5 mg catalyst in 5.0 mL H_2O, initial pressure 1.0 MPa ($CO_2/H_2 = 1:3$), and a reaction temperature ranging from 120 to 220 °C. No CO or other carbon-containing gases were detected through gas chromatography analysis. The liquid products from the CO_2 hydrogenation were quantified using ^1H nuclear magnetic resonance (NMR) spectroscopy, where only methanol and ethanol were detected. In the absence of Ir, methanol was the primary product over both In_2O_3 or P-In_2O_3 (Figure 3a). The introduction of P on In_2O_3 enhanced the methanol yield by 30 %. However, upon the introduction of atomically dispersed Ir species, ethanol becomes the primary product

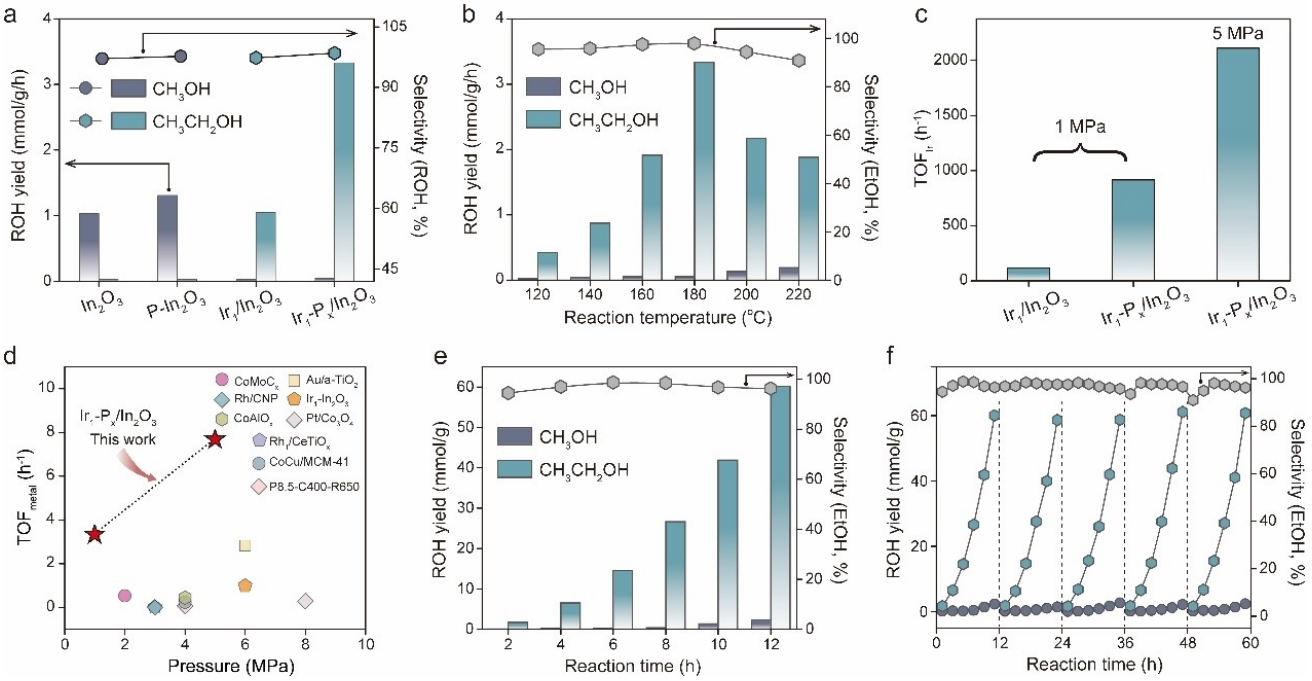

Figure 3. (a) Selectivity and yield of methanol and ethanol for In_2O_3, P-In_2O_3, Ir_1/In_2O_3 and Ir_1-P_x/In_2O_3. (b) Ethanol production over Ir_1-P_x/In_2O_3 under different temperatures. (c) TOF_{Ir} values of Ir_1/In_2O_3 and Ir_1-P_x/In_2O_3 at 1 MPa and 5 MPa. (d) Comparison for Ir_1-P_x/In_2O_3 with a series of recently reported CO_2-to-ethanol catalysts. (e) Effect of reaction time on the CO_2 hydrogenation over Ir_1-P_x/In_2O_3. (f) Cycling test for the CO_2 hydrogenation over Ir_1-P_x/In_2O_3.

over both Ir_1/In_2O_3 and Ir_1-P_x/In_2O_3, indicating that the atomically dispersed Ir species serve as efficient catalytic sites for facilitating C–C coupling. ; Supplementary comparison with Ir_1 supported on black phosphorus is presented in Figure S9 where nil ethanol is formed. The catalytic performance of Ir_1-P_x/In_2O_3 peaked at 180 °C, achieving an ethanol selectivity of 98.5 % and a yield of 3.33 mmol g_{cat}^{-1} h^{-1} after 8 h of time-on-stream (Figure 3b). The TOF_{Ir} of Ir_1-P_x/In_2O_3 reached 914 h^{-1}, which is 7.8 times that of Ir_1/In_2O_3 (116 h^{-1}) (Figure 3c). This observation suggests that P islands modulate the electronic structure of the Ir centers in the Ir_1-P_x entities, thereby facilitating C–C coupling at the Ir catalytic site. Further testing under more stringent pressure conditions demonstrated exceptional efficacy in the catalytic hydrogenation of CO_2 into ethanol (Table S4). For instance, at 5.0 MPa and 180 °C, the yield of Ir_1-P_x/In_2O_3 catalyst increased to 7.68 mmol g_{cat}^{-1} h^{-1} with 99 % selectivity of ethanol, and the TOF_{Ir} reached 2108 h^{-1}. Compared to reported literature (Figure 3d and Table S5), Ir_1-P_x/In_2O_3 exhibits, to the best of our knowledge, the best performance for CO_2 hydrogenation to ethanol. Moreover, the optimal temperatures for P-In_2O_3 and Ir_1-P_x/In_2O_3 were found to be 20 °C lower than those of their P-unmodified counterparts (Figure 3b and Figures S10–S11). To confirm the carbon source in the products, we conducted an isotope experiment using $^{13}CO_2/H_2$ as the feed gas, resulting in the exclusive formation $^{13}CH_3{}^{13}CH_2OH$ with a molecular ion peak at m/z = 46 (see Figure S12). Over extended reaction times with Ir_1-P_x/In_2O_3, both the methanol and ethanol yields showed slight increases (Figure 3e), while ethanol selectivity remained consistently around 99 %. In contrast, the ethanol selectivity for Ir_1/In_2O_3 noticeably decreased to about 80 % after 12 h of time-on-stream (Figure S13), indicating that the phosphorus species plays a key role in maintaining catalytic stability and durability for CO_2 hydrogenation to ethanol. In addition, Ir_1-P_x/In_2O_3 exhibited exceptional recycling stability, sustaining CO_2 hydrogenation for 5 cycles lasting 12 h each while maintaining 95 % of its initial catalytic activity (Figure 3f). Overall, Ir_1-P_x/In_2O_3 not only shows a significantly improved reaction rate for CO_2 hydrogenation but also effectively promotes C–C coupling, leading to efficient and stable ethanol production.

CO_2 Hydrogenation Reaction Mechanism of Ir_1-P_x/In_2O_3

To understand the mechanism by which Ir_1-P_x/In_2O_3 enhances the reaction rate and yield of ethanol, in situ diffuse reflectance infrared Fourier transform spectroscopy (DRIFTS) spectroscopy was employed, where key reaction intermediates during CO_2 hydrogenation can be observed. Initially, we conducted in situ DRIFTS to investigate the time-resolved profile of CO_2 adsorption. As shown in Figure 4a, a characteristic peak of *CO (~2070 cm^{-1}) was observed on both Ir_1/In_2O_3 (Figure S14) and Ir_1-P_x/In_2O_3, contrasting sharply with the spectra of In_2O_3 and P-In_2O_3 (Figure S15). This indicates the active role of Ir species for CO_2 adsorption and activation, consistent with the higher CO_2 conversion rates observed over both Ir_1/In_2O_3 and Ir_1-P_x/In_2O_3 catalysts. In addition, we noted significantly

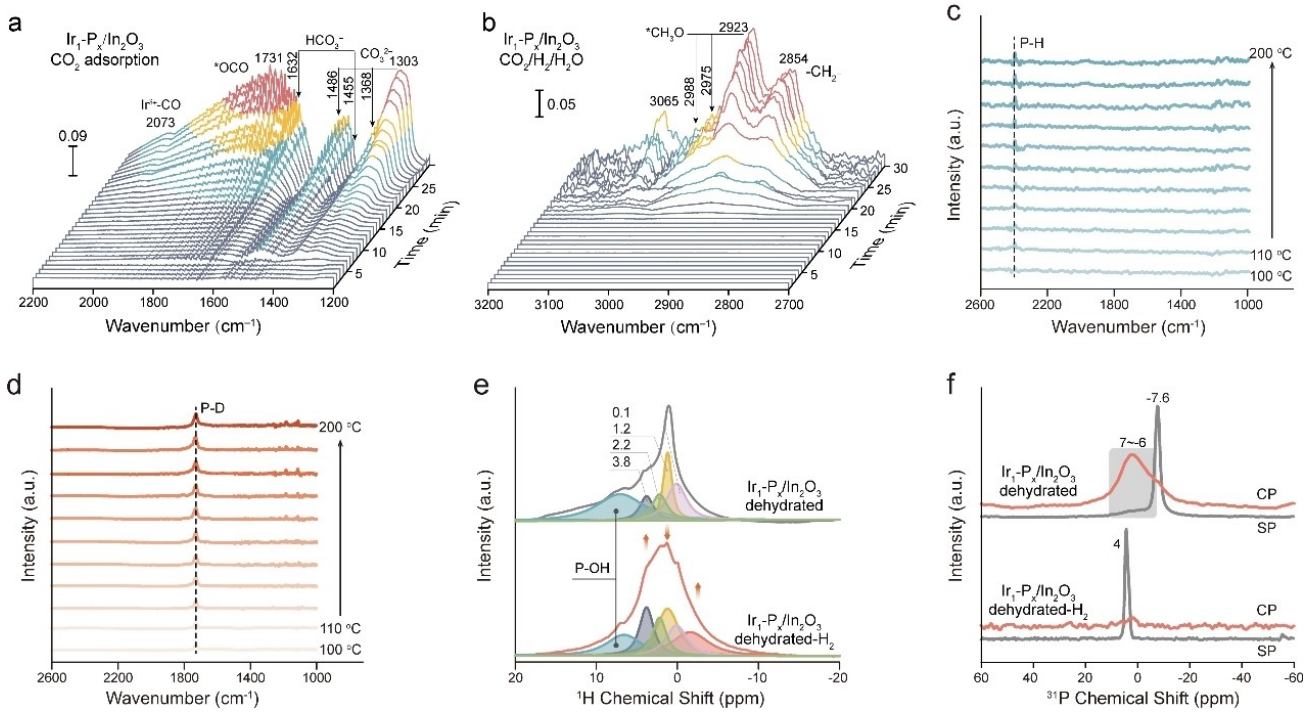

Figure 4. (a) In situ DRIFTS spectra of Ir_1-P_x/In_2O_3 exposed to CO_2 for 30 min at 180 °C. (b) In situ DRIFTS spectra of Ir_1-P_x/In_2O_3 under CO_2 hydrogenation condition for 30 min at 180 °C. In situ DRIFTS spectra of (c) H_2, (d) D_2 activation on Ir_1-P_x/In_2O_3 at 100–200 °C. (e) ^{1}H MAS SS NMR spectra of pristine dehydrated Ir_1-P_x/In_2O_3 before (top) and after (bottom) H_2 activation. (f) ^{31}P single-pulse (SP) and cross-polarization (CP) MAS SS NMR spectra of pristine dehydrated Ir_1-P_x/In_2O_3 before (top) and after (bottom) H_2 activation.

increased IR signal intensities from CO_2-related intermediates, such as bicarbonate (HCO_3^-) (1632, 1455 cm^{-1}) and carbonate (CO_3^{2-}) (1503, 1486, 1370, 1308 cm^{-1}) in the Ir-containing.[17] Furthermore, by comparing the CO_2 adsorption behavior over Ir_1/In_2O_3 and Ir_1-P_x/In_2O_3, we observed a rapid appearance of a strong *CO signal on the surface of Ir_1-P_x/In_2O_3 within 6 min. This suggests that Ir_1-P_x/In_2O_3 has superior CO_2 adsorption and activation abilities, likely attributed to the Ir_1-P_x entities. To obtain more detailed information, we conducted in situ DRIFTS measurements over Ir_1/In_2O_3 and Ir_1-P_x/In_2O_3 under a flow of $CO_2/H_2/H_2O$ (CO_2:H_2 = 1:3, bubbled in aqueous solution) at 180 °C (Figure 4b and Figure S16). A strong IR peak at 2923 cm^{-1}, characteristic of the key intermediate methoxy (*CH_3O) species, was observed in both Ir_1/In_2O_3 and Ir_1-P_x/In_2O_3.[18] In contrast, the IR peak attributable to *CH_3O in Ir_1/In_2O_3 was much weaker. Overall, the in situ DRIFTS experiments identified the presence of Ir-CO* and CH_3O*, which are key intermediate species commonly observed during CO_2 hydrogenation.[19]

Another critical step is the activation of hydrogen, which is essential for the hydrogenation of adsorbed CO_2 species. To further understand H_2 activation over Ir_1-P_x/In_2O_3, we employed in situ DRIFTS to examine the adsorption behavior of H_2/D_2 on the catalyst surface. As shown in Figure 4c, a distinct IR signal appears in Ir_1-P_x/In_2O_3 at approximately 2400 cm^{-1} between 100–200 °C under an H_2 atmosphere, corresponding to the stretching of P–H_{ads}.[20] With increasing reaction temperature, the intensity of this IR peak increases, indicating a higher coverage of P–H_{ads} intermediates. Using the isotope D_2, we further substantiated the assignment of the 2400 cm^{-1} vibration, as depicted in Figure 4d. We observed a shift of the P-D_{ads} bond to 1740 cm^{-1}, consistent with Hooke's law.[21] Additionally, the H_2 temperature-programmed reduction experiment (H_2-TPR, Figure S17) revealed that P-In_2O_3 and Ir_1-P_x/In_2O_3 exhibited lower hydrogen reduction temperatures compared to In_2O_3 and Ir_1/In_2O_3, highlighting the strong hydrogen activation properties exhibited through P modification, which aligns with our previous findings.[11] Importantly, we did not observe any noticeable IR vibrational peaks corresponding to hydrogen decomposition in Ir_1/In_2O_3 (Figure S18), indicating that the activation of hydrogen in Ir_1/In_2O_3 could be more challenging under the same conditions. This further suggests that Ir_1-P_x/In_2O_3 has a higher propensity for hydrogen activation, particularly at the P sites. It is well known that precious metals, especially Pt and Pd, effectively activate hydrogen by forming metal-hydride species.[22] However, the absence of an Ir–H IR signal in multiple DRIFTS measurements implies that the contribution of Ir to hydrogen activation could be relatively limited. This observation aligns with literature findings indicating that the formation of Ir–H bonds from H_2 cleavage typically requires a higher energy input, than what is provided under the current measurement conditions.[23]

To further investigate the chemical states of the hydride and phosphorus species, as well as to determine whether the Ir sites are directly involved in hydrogen activation through

the formation of Ir–H bonds, we conducted solid-state NMR (SS NMR) spectroscopy experiments. The SS NMR results are presented in Figure 4e, where peaks at 0.1, 1.2, 2.2, and 3.8 ppm can be assigned to terminal (M-OH), bridged ($M_2(\mu_2$-OH); 1.2 and 2.2 ppm), and triply bridged hydroxy ($M_3(\mu_3$-OH)) species, respectively.[24] The strong correlation peaks between these signals in the two-dimensional ^{1}H-^{1}H exchange spectrum (Figure S19) indicate that these surface hydroxy groups are in close proximity, forming a complex hydroxy network. Additionally, a broad peak centered around 8 ppm is observed in Figure 4e. Since this peak is distant from the metal hydroxy species (Figure S20) but shows a strong correlation with ^{31}P species (Figure S17), it can be assigned to P–OH species, supported by a study by Pourpoint et al.[25] The ^{31}P magic-angle spinning (MAS) SS NMR spectrum of pristine dehydrated Ir_1-P_x/In_2O_3 suggests the presence of two types of phosphorus species: a sharp peak at −7.6 ppm and a broad peak around 7~−6 ppm. The former peak likely corresponds to bulk phosphorus species or fully coordinated P without OH, while the latter peak, whose intensity is greatly enhanced in the cross-polarization (CP) spectrum, is attributed to hydroxylated P ('P–OH') species, consistent with the 2D ^{31}P-^{1}H spectrum (Figure S20). After the adsorption of H_2 followed by high-temperature treatment at 200 °C, the intensity of the P–OH peak significantly decreases in the ^{1}H MAS SS NMR spectrum (Figure 4e), and this P–OH contribution becomes negligible in the ^{31}P CP MAS SS NMR spectrum (Figure 4f). This clearly implies the consumption of P–OH through reaction with H_2, which is likely regenerated in the presence of water under reaction conditions. We also observed a notable shift in the ^{31}P peak in the single-pulse (SP) spectrum from −7.6 ppm to 4.0 ppm after H_2 treatment, indicating the chemical reduction of the phosphorus species. The absence of NMR evidence for Ir–H bonds further support the limited role of Ir in hydrogen activation within this system.

We subsequently performed DFT calculations to study how Ir_1-P_x significantly enhanced the conversion of CO_2 to ethanol. As shown in Figure 5a and Figure S21, we considered four types of catalytic sites for hydrogen activation. Notably, the P/P–OH sites exhibit the lowest hydrogen activation energy. This process involves the consumption of –OH groups at the P/P–OH sites by hydrogen, resulting in the formation of free water, P/P sites, and P–H species, which aligns with the chemical reduction of P observed in the SS NMR data. Among the Ir/P, P/P, and Ir sites, the P/P sites demonstrate superior effectiveness for hydrogen activation, outperforming the Ir site. As a result, enhancing H_2 dissociation through catalytic sites containing P is expected to improve the kinetics of CO_2 hydrogenation toward ethanol production. Figure 5b and 5c illustrate the calculated Gibbs free energy (ΔG) of CO_2 hydrogenation to ethanol over Ir_1/In_2O_3 and Ir_1-P_x/In_2O_3, including the relevant intermediates. This process involves the adsorption and

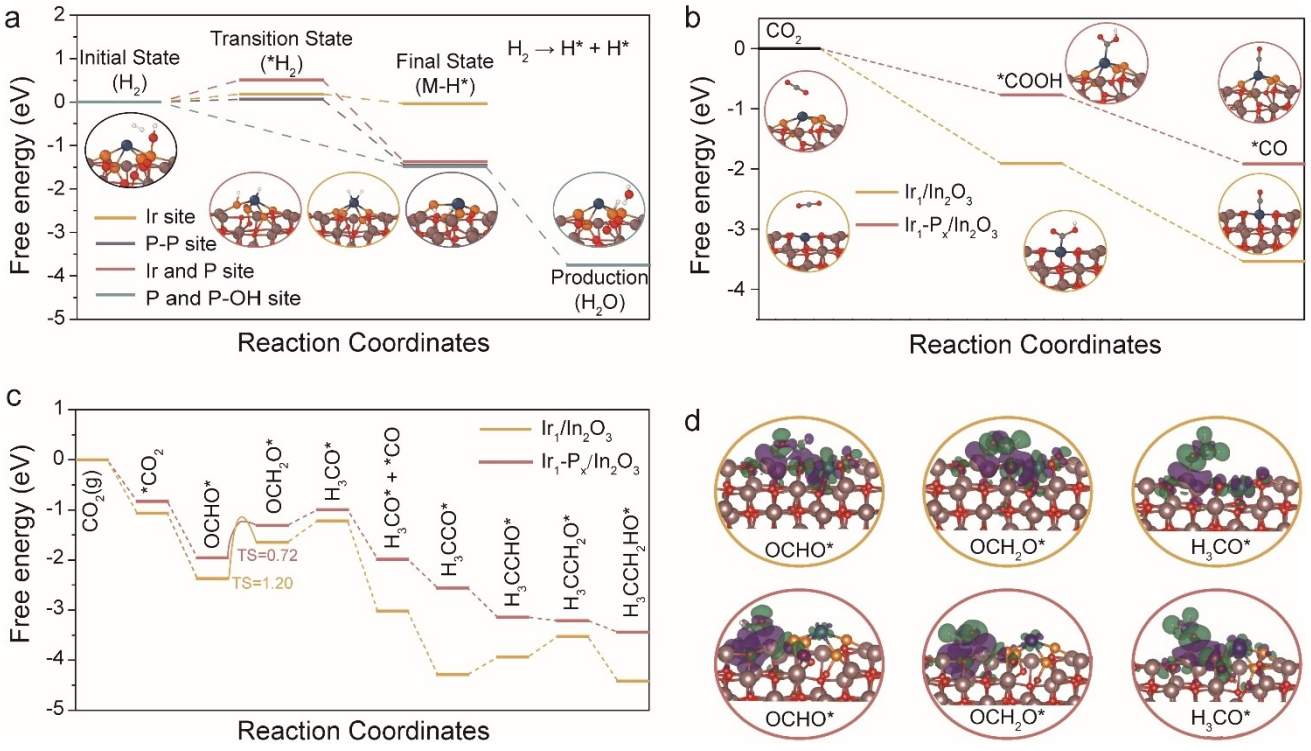

Figure 5. DFT calculations. (a) Energy diagram for the process $H_2 \rightarrow H^* + H^*$ occurring at Ir/P sites (red), P/P–OH sites (blue), P/P sites (purple), and Ir sites (yellow) on Ir_1-P_x/In_2O_3. (b) Gibbs free energy (ΔG) of CO_2 reduction to CO at the Ir active site, along with the corresponding crystal structures of Ir_1/In_2O_3 and Ir_1-P_x/In_2O_3, as calculated by the GGA/PBE level. (c) Calculated ΔG diagrams of CO_2 reduction to ethanol on Ir_1/In_2O_3 and Ir_1-P_x/In_2O_3. (d) Charge density differences of the (top) Ir_1/In_2O_3 and (bottom) Ir_1-P_x/In_2O_3 surfaces after molecular deposition (purple and green regions indicate electron accumulation and depletion, respectively).

activation of CO_2 on the Ir site, followed by the insertion of a carbonyl (*CO) on $*CH_3O$, as confirmed by our in situ DRIFTS analysis and supporting literature.[26] Our DFT calculations indicate that CO_2 adsorption and activation to *CO on both Ir_1/In_2O_3 and Ir_1-P_x/In_2O_3 are spontaneous (Figure 5b). As shown in Figure 5c and 5d, the hydrogenation of *OCHO to $*OCH_2O$ emerges as a key rate-limiting step (RLS) in the CO_2 hydrogenation process, while the carbonyl insertion process on the Ir sites is exothermic. For Ir_1-P_x/In_2O_3, the ΔG of the RLS is 0.65 eV, which is lower than the 0.73 eV observed for Ir_1/In_2O_3, indicating that Ir_1-P_x on In_2O_3 can reduce the energy barrier for CO_2 hydrogenation to ethanol. In addition, the transition state energy calculations for the key reaction step *OCHO→ $*OCH_2O$ on the Ir_1/In_2O_3 and Ir_1-P_x/In_2O_3 systems are shown in Figure 5c. The transition state energy for Ir_1/In_2O_3 is calculated to be 1.23 eV, whereas the transition state energy for Ir_1-P_x/In_2O_3 is reduced to 0.72 eV. This finding further demonstrates that the introduction of P effectively lowers the energy barrier for this reaction step, thereby facilitating an accelerated reaction process. As seen in Figure S22 and S23, a significant alteration in electronic structures is evident, by analyzing the projected density of states (PDOS), upon the adsorption of $*CO_2$, *OCHO, $*OCH_2O$, $*OCH_3$, and $*CH_3CHO$ absorbed on Ir_1/In_2O_3 and Ir_1-P_x/In_2O_3.

Conclusion

In summary, this study presents an innovative SAC that is precisely deposited onto a specific entity on a catalyst surface. This catalyst exhibits outstanding catalytic activity in the hydrogenation of CO_2. Under conditions of 180 °C and 1 MPa ($CO_2/H_2 = 1:3$), we achieved an ethanol yield of 3.3 $mmol\,g^{-1}\,h^{-1}$ over 8 h, with a remarkable selectivity of 98.5 % and a TOF_{Ir} of up to 914 h^{-1}. When the reaction pressure is increased to 5 MPa, the TOF_{Ir} rises significantly to 2108 h^{-1}. Combined experimental and computation findings reveal that the introduction of the P cluster islands into the catalytic system has a dual impact on the CO_2 hydrogenation process. First, the P sites enhance hydrogen activation. Second, the coordination between Ir and P atoms modifies the catalytic environment, effectively lowering the energy barrier for the RLS in CO_2 hydrogenation, making Ir_1-P_x/In_2O_3 achieve excellent catalytic performance at low pressure. This synergistic effect leads to a substantial enhancement in the reaction rate of CO_2 hydrogenation to ethanol, highlighting the potential of Ir_1-P_x/In_2O_3 as a highly efficient catalyst for sustainable chemical production. These findings not only contribute valuable insights into the design of SACs but also suggest promising pathways for future research in catalyst optimization and support material modifications.

Acknowledgements

This work was financially supported by the National Natural Science Foundation of China (22172136, and 22475145), the Hong Kong Research Grants Council (15305722, 15301521, 25300823, and 15300724), PolyU fund (P0042930, P0039335, P0042646, P0050410, and P0053682), and Environment and Conservation Fund (ECF 44/2023) . We thank NSRRC (2020-2-030-1), and SPring-8 (2022B0545, 2023B1665, and 2023B1666) for beamtimes; UMF, UCEA, ULS of HKPU for the support in material characterization. L. Liu and S. Zheng conceived and designed the experiments. L. Liu, X. Shi carried out the synthesis of catalysts and performed experiments on electrochemical testing. L. Liu, G. Li, H. B. Yang and T. W. Lo contributed to the data analysis. J. Liu and J. Yin performed the DFT calculation. G. Li performed the SS NMR measurements. K.F. Yung contributed to the project discussion. H. B. Yang and T. W. B. Lo supervised the entire project.

Conflict of Interest

The authors declare no conflict of interest.

Data Availability Statement

Research data are not shared.

Keywords: guided deposition · Ir_1-P_x · CO_2 hydrogenation · H_2 activation · ethanol

[1] a) Y. Y. Birdja, E. Pérez-Gallent, M. C. Figueiredo, A. J. Göttle, F. Calle-Vallejo, M. T. M. Koper, *Nat. Energy* **2019**, *4*, 732–745; b) S. Dang, B. Qin, Y. Yang, H. Wang, J. Cai, Y. Han, S. Li, P. Gao, Y. Sun, *Sci. Adv.* **2020**, *6*, eaaz2060; c) J. Zhang, W. Cai, F. X. Hu, H. Yang, B. Liu, *Chem. Sci.* **2021**, *12*, 6800–6819; d) F. Raziq, C. Feng, M. Hu, S. Zuo, M. Z. Rahman, Y. Yan, Q.-H. Li, J. Gascon, H. Zhang, *J. Am. Chem. Soc.* **2024**, *146*, 21008–21016.

[2] a) J. Ding, H. Yang, X.-L. Ma, S. Liu, W. Liu, Q. Mao, Y. Huang, J. Li, T. Zhang, B. Liu, *Nat. Energy* **2023**, *8*, 1386–1394; b) J. Ding, F. Li, J. Zhang, Q. Zhang, Y. Liu, W. Wang, W. Liu, B. Wang, J. Cai, X. Su, H. B. Yang, X. Yang, Y. Huang, Y. Zhai, B. Liu, *J. Am. Chem. Soc.* **2023**, *145*, 11829–11836; c) W. Ma, S. Xie, T. Liu, Q. Fan, J. Ye, F. Sun, Z. Jiang, Q. Zhang, J. Cheng, Y. Wang, *Nat. Catal.* **2020**, *3*, 478–487; d) J. Zhang, J. Ding, Y. Liu, C. Su, H. Yang, Y. Huang, B. Liu, *Joule* **2023**, *7*, 1700–1744; e) X. Zhang, W. Huang, L. Yu, M. García-Melchor, D. Wang, L. Zhi, H. Zhang, *Carbon Energy* **2024**, *6*, e362.

[3] a) K. Zheng, Y. Li, B. Liu, F. Jiang, Y. Xu, X. Liu, *Angew. Chem. Int. Ed.* **2022**, *61*, e202210991; b) B. An, Z. Li, Y. Song, J. Zhang, L. Zeng, C. Wang, W. Lin, *Nat. Catal.* **2019**, *2*, 709–717; c) Y. Wang, W. Wang, R. He, M. Li, J. Zhang, F. Cao, J. Liu, S. Lin, X. Gao, G. Yang, M. Wang, T. Xing, T. Liu, Q. Liu, H. Hu, N. Tsubaki, M. Wu, *Angew. Chem. Int. Ed.* **2023**, *62*, e202311786; d) S. S. Ali, S. S. Ali, N. Tabassum, *J. Environ. Chem. Eng.* **2022**, *10*, 106962.

[4] a) C. Zhou, A. Aitbekova, G. Liccardo, J. Oh, M. L. Stone, E. J. McShane, B. Werghi, S. Nathan, C. Song, J. Ciston, K. C. Bustillo, A. S. Hoffman, J. Hong, J. Perez-Aguilar, S. R. Bare, M. Cargnello, *Angew. Chem. Int. Ed.* **2024**, *n/a*, e202406761; b) H. Guo, H. Zhu, G.-Y. Liu, Z.-X. Chen, *ACS Catal.* **2024**, *14*, 5720–5734.

[5] a) D. Wang, Q. Bi, G. Yin, W. Zhao, F. Huang, X. Xie, M. Jiang, *Chem. Commun.* **2016**, *52*, 14226–14229; b) J. Chen, Y. Zha, B. Liu, Y. Li, Y. Xu, X. Liu, *ACS Catal.* **2023**, *13*, 7110–7121; c) C.-C. Tran, S. Kaliaguine, *Chem. Eng. J.* **2024**, *496*, 153636.

[6] X. Ye, C. Yang, X. Pan, J. Ma, Y. Zhang, Y. Ren, X. Liu, L. Li, Y. Huang, *J. Am. Chem. Soc.* **2020**, *142*, 19001–19005.

[7] a) B. Han, Y. Guo, Y. Huang, W. Xi, J. Xu, J. Luo, H. Qi, Y. Ren, X. Liu, B. Qiao, T. Zhang, *Angew. Chem. Int. Ed.* **2020**, *59*, 11824–11829; b) H. Xin, L. Lin, R. Li, D. Li, T. Song, R. Mu, Q. Fu, X. Bao, *J. Am. Chem. Soc.* **2022**, *144*, 4874–4882; c) X. Li, X. I. Pereira-Hernández, Y. Chen, J. Xu, J. Zhao, C.-W. Pao, C.-Y. Fang, J. Zeng, Y. Wang, B. C. Gates, J. Liu, *Nature* **2022**, *611*, 284–288; d) W. Huang, T. Bo, S. Zuo, Y. Wang, J. Chen, S. Ould-Chikh, Y. Li, W. Zhou, J. Zhang, H. Zhang, *SusMat* **2022**, *2*, 466–475.

[8] a) C. K. T. Wun, Z. Wang, S. Kawaguchi, S. Kobayashi, T.-S. Wu, T. Chen, C. Lin, C. C. Tang, J. Yin, T. W. B. Lo, *J. Mater. Chem. A* **2024**, *12*, 25442–25448; b) Q. Wang, H. Wang, H. Cao, C.-W. Tung, W. Liu, S.-F. Hung, W. Wang, C. Zhu, Z. Zhang, W. Cai, Y. Cheng, H. B. Tao, H. M. Chen, Y.-G. Wang, Y. Li, H. B. Yang, Y. Huang, J. Li, B. Liu, *Nat. Catal.* **2023**, *6*, 916–926.

[9] a) J. Ding, F. Li, J. Zhang, H. Qi, Z. Wei, C. Su, H. B. Yang, Y. Zhai, B. Liu, *Adv. Mater.* **2023**, *36*, 2306480; b) K. Zheng, Y. Li, B. Liu, J. Chen, Y. Xu, Z. Li, X. Liu, *Appl. Catal. B* **2024**, *346*, 123730.

[10] F. Lei, Y. Sun, K. Liu, S. Gao, L. Liang, B. Pan, Y. Xie, *J. Am. Chem. Soc.* **2014**, *136*, 6826–6829.

[11] Z. Wei, J. Ding, Z. Wang, A. Wang, L. Zhang, Y. Liu, Y. Guo, X. Yang, Y. Zhai, B. Liu, *Angew. Chem. Int. Ed.* **2024**, *63*, e202402070.

[12] a) J. Ding, Z. Teng, X. Su, K. Kato, Y. Liu, T. Xiao, W. Liu, L. Liu, Q. Zhang, X. Ren, J. Zhang, Z. Chen, O. Teruhisa, A. Yamakata, H. Yang, Y. Huang, B. Liu, Y. Zhai, *Chem* **2023**, *9*, 1017–1035; b) J. Ding, Z. Wei, F. Li, J. Zhang, Q. Zhang, J. Zhou, W. Wang, Y. Liu, Z. Zhang, X. Su, R. Yang, W. Liu, C. Su, H. B. Yang, Y. Huang, Y. Zhai, B. Liu, *Nat. Commun.* **2023**, *14*, 6550.

[13] Y. Liu, X. Su, J. Ding, J. Zhou, Z. Liu, X. Wei, H. B. Yang, B. Liu, *Chem. Soc. Rev.* **2024**.

[14] a) J. Wei, H. Tang, L. Sheng, R. Wang, M. Fan, J. Wan, Y. Wu, Z. Zhang, S. Zhou, J. Zeng, *Nat. Commun.* **2024**, *15*, 559; b) J. Wei, H. Tang, Y. Liu, G. Liu, L. Sheng, M. Fan, Y. Ma, Z. Zhang, J. Zeng, *Angew. Chem. Int. Ed.* **2024**, *63*, e202410520.

[15] a) Y. Yang, X. Zhao, H.-E. Wang, M. Li, C. Hao, M. Ji, S. Ren, G. Cao, *J. Mater. Chem. A* **2018**, *6*, 3479–3487; b) H. Bin Yang, C.-Q. Xu, S. Baskaran, Y.-R. Lu, C. Gu, W. Liu, J. Ding, J. Zhang, Q. Wang, W. Chen, J. Li, Y. Huang, T. Zhang, B. Liu, *EES Catalysis* **2023**, *1*, 774–783.

[16] Y.-F. Yang, H.-Q. Huang, Z.-Y. Song, H.-Q. Li, X.-Y. Yu, Y.-M. Cui, M. Yang, S.-H. Chen, X.-J. Huang, *Environ. Sci.-Nano* **2023**, *10*, 800–811.

[17] a) L. Wang, L. Wang, J. Zhang, X. Liu, H. Wang, W. Zhang, Q. Yang, J. Ma, X. Dong, S. J. Yoo, J.-G. Kim, X. Meng, F.-S. Xiao, *Angew. Chem. Int. Ed.* **2018**, *57*, 6104–6108; b) S. Bai, Q. Shao, P. Wang, Q. Dai, X. Wang, X. Huang, *J. Am. Chem. Soc.* **2017**, *139*, 6827–6830; c) S. Liu, Y. He, W. Fu, J. Ren, J. Chen, H. Chen, R. Sun, Z. Tang, C. Mebrahtu, F. Zeng, *Appl. Catal. A* **2024**, *670*, 119549.

[18] a) Z. Wang, C. Yang, X. Li, X. Song, C. Pei, Z.-J. Zhao, J. Gong, *Nano Res.* **2023**, *16*, 6128–6133; b) S. Ji, F. Hong, D. Mao, Q. Guo, J. Yu, *Chem. Eng. J.* **2024**, *495*, 153633; c) O. Martin, A. J. Martin, C. Mondelli, S. Mitchell, T. F. Segawa, R. Hauert, C. Drouilly, D. Curulla-Ferre, J. Perez-Ramirez, *Angew. Chem. Int. Ed.* **2016**, *55*, 6261–6265.

[19] K. Zheng, Y. Li, H. He, B. Liu, Y. Xu, X. Liu, *J. Catal.* **2024**, *440*, 118532.

[20] a) C. Wu, S. Ding, D. Liu, D. Li, S. Chen, H. Wang, Z. Qi, B. Ge, L. Song, *Research* **2020**, *2020*, 5860712; b) C. Li, C. Tian, H. Tang, M. Liu, L. Zheng, F. Huang, G.-R. Li, Q. Li, *ACS Energy Lett.* **2023**, *8*, 5161–5169.

[21] Y. Liu, Z. Wei, X. Su, X. Shi, L. Liu, T. Wang, X. Xu, M. Zhao, Y. Zhai, H. B. Yang, B. Liu, *Adv. Funct. Mater.* **2024**, 2403547.

[22] a) D. Paleček, G. Tek, J. Lan, M. Iannuzzi, P. Hamm, *J. Phys. Chem. Lett.* **2018**, *9*, 1254–1259; b) J. N. Kondo, S. Ge, T. Suzuki, R. Osuga, T. Matsumoto, T. Yokoi, Y. Shimizu, A. Fukazawa, N. Shida, M. Atobe, *J. Phys. Chem. C* **2022**, *126*, 19376–19385.

[23] a) J. Fu, J. Dong, R. Si, K. Sun, J. Zhang, M. Li, N. Yu, B. Zhang, M. G. Humphrey, Q. Fu, J. Huang, *ACS Catal.* **2021**, *11*, 1952–1961; b) Q. Shen, H. Jin, P. Li, X. Yu, L. Zheng, W. Song, C. Cao, *Nano Res.* **2022**, *15*, 5024–5031; c) W. Gao, S. Liu, G. Sun, C. Zhang, Y. Pan, *Small* **2023**, *19*, 2300956.

[24] Q. Han, P. Gao, L. Liang, K. Chen, A. Dong, Z. Liu, X. Han, Q. Fu, G. Hou, *Anal. Chem.* **2021**, *93*, 16769–16778.

[25] F. Pourpoint, C. C. Diogo, C. Gervais, C. Bonhomme, F. Fayon, S. L. Dalicieux, I. Gennero, J.-P. Salles, A. P. Howes, R. Dupree, J. V. Hanna, M. E. Smith, F. Mauri, G. Guerrero, P. Hubert Mutin, D. Laurencin, *J. Mater. Res.* **2011**, *26*, 2355–2368.

[26] a) Z. He, Q. Qian, J. Ma, Q. Meng, H. Zhou, J. Song, Z. Liu, B. Han, *Angew. Chem. Int. Ed.* **2016**, *55*, 737–741; b) C. Yang, R. Mu, G. Wang, J. Song, H. Tian, Z.-J. Zhao, J. Gong, *Chem. Sci.* **2019**, *10*, 3161–3167; c) L. Ding, T. Shi, J. Gu, Y. Cui, Z. Zhang, C. Yang, T. Chen, M. Lin, P. Wang, N. Xue, L. Peng, X. Guo, Y. Zhu, Z. Chen, W. Ding, *Chem* **2020**, *6*, 2673–2689.

Manuscript received: November 22, 2024
Accepted manuscript online: January 21, 2025
Version of record online: February 3, 2025